

Article

# The Impacts of Matrix Compositions on Nanopore Structure and Fractal Characteristics of Lacustrine Shales from the Changling Fault Depression, Songliao Basin, China

Zhuo Li <sup>1,2</sup>, Zhikai Liang <sup>1,2,\*</sup>, Zhenxue Jiang <sup>1,2</sup>, Fenglin Gao <sup>1,2</sup>, Yinghan Zhang <sup>1,2</sup>, Hailong Yu <sup>1,2</sup>, Lei Xiao <sup>1,2</sup> and Youdong Yang <sup>1,2</sup>

<sup>1</sup> State Key Laboratory of Petroleum Resources and Prospecting, China University of Petroleum (Beijing), Beijing 102249, China; zhuo.li@cup.edu.cn (Z.L.); jiangzhenxue0405@163.com (Z.J.); feilaifeng2011@gmail.com (F.G.); zhangyinghan2021@163.com (Y.Z.); yhl2017210211@163.com (H.Y.); xlcupb@163.com (L.X.); yydzgsydxj@163.com (Y.Y.)

<sup>2</sup> Unconventional Natural Gas Research Institute, China University of Petroleum (Beijing), Beijing 102249, China

\* Correspondence: liangzhikai2020@163.com; Tel.: +86-010-89739051

Received: 13 January 2019; Accepted: 15 February 2019; Published: 22 February 2019



**Abstract:** The Lower Cretaceous Shahezi shales are the targets for lacustrine shale gas exploration in Changling Fault Depression (CFD), Southern Songliao Basin. In this study, the Shahezi shales were investigated to further understand the impacts of rock compositions, including organic matters and minerals on pore structure and fractal characteristics. An integrated experiment procedure, including total organic carbon (TOC) content, X-ray diffraction (XRD), field emission-scanning electron microscope (FE-SEM), low pressure nitrogen physisorption (LPNP), and mercury intrusion capillary pressure (MICP), was conducted. Seven lithofacies can be identified according to on a mineralogy-based classification scheme for shales. Inorganic mineral hosted pores are the most abundant pore type, while relatively few organic matter (OM) pores are observed in FE-SEM images of the Shahezi shales. Multimodal pore size distribution characteristics were shown in pore width ranges of 0.5–0.9 nm, 3–6 nm, and 10–40 nm. The primary controlling factors for pore structure in Shahezi shales are clay minerals rather than OM. Organic-medium mixed shale (OMMS) has the highest total pore volumes (0.0353 mL/g), followed by organic-rich mixed shale (ORMS) (0.02369 mL/g), while the organic-poor shale (OPS) has the lowest pore volumes of 0.0122 mL/g. Fractal dimensions  $D_1$  and  $D_2$  (at relative pressures of 0–0.5 and 0.5–1 of LPNP isotherms) were obtained using the Frenkel–Halsey–Hill (FHH) method, with  $D_1$  ranging from 2.0336 to 2.5957, and  $D_2$  between 2.5779 and 2.8821. Fractal dimensions are associated with specific lithofacies, because each lithofacies has a distinctive composition. Organic-medium argillaceous shale (OMAS), rich in clay, have comparatively high fractal dimension  $D_1$ . In addition, organic-medium argillaceous shale (ORAS), rich in TOC, have comparatively high fractal dimension  $D_2$ . OPS shale contains more siliceous and less TOC, with the lowest  $D_1$  and  $D_2$ . Factor analysis indicates that clay contents is the most significant factor controlling the fractal dimensions of the lacustrine Shahezi shale.

**Keywords:** Changling Fault Depression; Shahezi Formation; fractal dimensions; pore structure; shale lithofacies; lacustrine shales

### 1. Introduction

Organic shales commonly contain complex matrix compositions (organic matters and minerals) and nanopore pore networks, various pore types, and multiscale pore width [1–4]. Scanning electron microscopy, small angle scattering, nuclear magnetic resonance, low pressure gas physisorption, and high-pressure mercury intrusion methods can be used to characterize pore structure in organic shales [1,2,5–10]. Among these methods, low pressure nitrogen physisorption (LPNP) is proposed to be an effective method for characterizing pore structure and fractal dimensions in organic shales [2,11–16]. Fractal theory was proposed [17] and used to study the properties of porous materials and pores with irregular surfaces and shapes [18–20]. Fractal dimensions were applied to study pore geometries and pore size distribution in coals and shales [2,9,20–23]. Lithofacies may refer to the homogeneity of specific geochemical, geological, mineralogical, and petrophysical characteristics of rocks [24]. Shale lithofacies may represent the spatial variations in organic matter richness, and shale properties [25]. Lithofacies classification is also an effective technique to identify favorable shale gas targets [26]. Previous studies about the shale lithofacies, pore structure and fractal characteristics were mainly focused on marine shales [4,13,15,25–29]. Therefore, shale lithofacies and their impacts on pore structure and fractal dimensions of lacustrine shales need further investigation. Lithofacies classification, shale reservoir characteristics, and main controlling factors of pore structure of the lacustrine shales from the Lower Cretaceous Shahezi Formation in the Changling Fault Depression (CFD) of the Songliao Basin have been studied [30]. However, the relationships of pore structure and fractal dimensions with shale lithofacies of the Shahezi shales were still poorly correlated.

In the present work, the Shahezi Shales in CFD were investigated to reveal the impacts of shale compositions on nanopore structure and fractal characteristics (Figure 1). The CFD experienced three successive evolution stages including Early Cretaceous rifting (extensional) stage, Late Cretaceous depression stage, and Latest Cretaceous to Quaternary uplifting stage can be confirmed [31–33]. The Shahezi (K<sub>1</sub>sh) shales consist of deep lake and semi-deep lake sediments, which are the main source rock of the gas accumulated within the gas fields (Ro > 2%) in the study area [34]. The predominant macerals type is vitrinite (82.1%–96.7%) and the main organic type of kerogen is type III of the Shahezi shales [30,34].

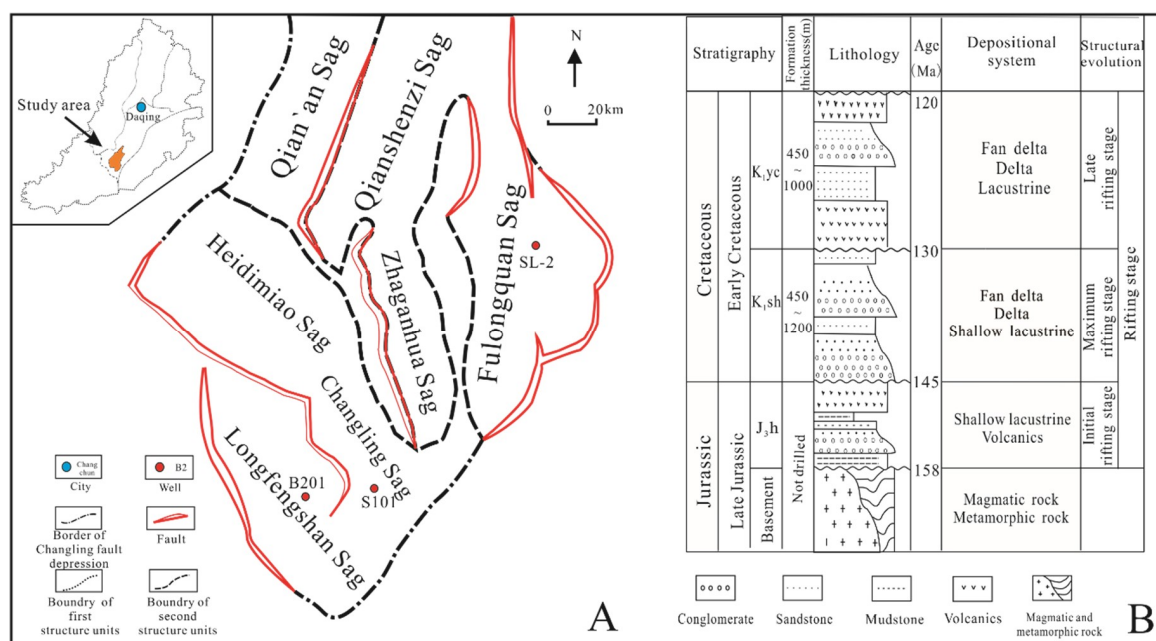


**Figure 1.** (A) Maps showing the location and the structure distributions in the Changling Fault Depression (CFD); (B) stratigraphy column showing petrology and depositional facies of the Shahezi Formation in CFD (modified after Gao et al., 2018 [30] and Cai et al., 2017 [31]).

The objectives of this paper are to: (1) identify shale lithofacies based on a mineralogy-based classification scheme for shales; (2) characterize pore structures of each shale lithofacies; (3) calculate fractal dimensions obtain from LPNP isotherms using FHH method; (4) investigate of the impacts of lithofacies on pore structure and fractal dimensions of lacustrine shales in CFD, Songliao Basin.

## 2. Materials and Methods

A total of twenty-two selected shale samples were obtained from the lower Cretaceous Shahezi Formation in Wells S-101, SL-2 and B-201. The depths are in the ranges of 2392–2577 m and 3430–3943 m, respectively (Table 1). An integrated experiment procedure, including total organic carbon (TOC), X-ray diffraction (XRD), field emission scanning electron microscope (FE-ESEM), and low pressure nitrogen physisorption (LPNP), was conducted.

The TOC content, Rock-Eval and bulk XRD composition measurements were conducted at China University of Petroleum (Beijing). TOC contents were determined by a Leco CS230 carbon/sulfur analyzer (LECO Corporation, St Joseph, MI, USA). Shale samples were treated with hydrochloric acid for two hours. Then the samples were washed out using distilled water and dried before the TOC content analysis. Rock-Eval analysis was carried out using OGE-II rock pyrolyzer (RIPED, Beijing, China) under programmed heating processes. The vitrinite reflectance ( $R_o$ ) values were calculated by Rock-Eval pyrolysis parameters based on the formula of Jarvie et al. (2001) [35]. The kerogen type was determined by cross-plots of hydrogen index (HI) against maximum cracking temperature ( $T_{max}$ ) and residual hydrocarbon ( $S_2$ ) versus TOC [36]. Bulk mineral compositions were determined using a Bruker D8 DISCOVER XRD diffractometer (BRUKER AXS Corporation, Karlsruhe, Germany) using Co Ka-radiation at 45 kV. Quantitative analysis was performed by Rietveld refinement, with customized Ufer models [37].

Ar-ion milling surface of shale samples was prepared on a Hitachi IM4000 apparatus for 2 h before FE-SEM imaging. FE-SEM observation and imaging were conducted using a Zeiss SUPRA 55 Sapphire FE-SEM (Carl Zeiss, Heidenheim, Germany) equipped with secondary electron (SE), backscattered electron (BSE) detectors and an energy dispersive spectrometer at Institute of Geology and Geophysics, Chinese Academy of Sciences. Image-Pro Plus software (Image-Pro<sup>®</sup> Plus, Media Cybernetics, Rockville, MD, USA) was used for image analysis on shale samples. FE-SEM images were initially transformed to an eight-bit bitmap, then, OM and mineral grains were filtered from transformed SEM images via a color threshold. Finally, the pore binary images were extracted and quantitatively analyzed for pore characteristics.

LPNP experiments were conducted at the Beijing Center for Physical and Chemical Analysis with a Quantachrome NOVA 4200e (Quantachrome, Boynton Beach, FL, USA) following Chinese National Standard GB/T31483-2015. The samples were dried at 110 °C for 12 h before the experiment to remove moisture. The parameters were set at −196.15 °C, with relative pressure range from 0.001 to 0.998. The specific surface area was calculated by the multipoint BET (Brunauer–Emmett–Teller) method and the pore size distribution and pore volume were calculated using the Barrette–Joyner–Halenda (BJH) theory. the FHH model [18] for fractal dimensions calculation can be expressed as:

$$\ln V = (D - 3) \times \ln(\ln P_0/P) + C \quad (1)$$

where  $P$  is the equilibrium pressure,  $V$  is the volume corresponding to the equilibrium pressure  $P$ ;  $D$  is the fractal dimension,  $C$  is the parameter, and  $P_0$  is the saturation pressure.

The mercury intrusion capillary pressure (MICP) measurements were performed on a Micromeritics Autopore IV 9500 equipment (Micromeritics, Atlanta, GA, USA) at China University of Mining and Technology, with an operating pressure up to 30,000 Psi and the measurable pores ranging from 5.4 nm to 200  $\mu\text{m}$  [30].

**Table 1.** Mineral and geochemical compositions of the Shahezi shale in CFD.

No.	Sample ID	Well ID	Depth (m)	Lithofacies	Mineral Composition (%)					Geochemical Composition (%)					
					Quartz	Feldspar	Calcite	Pyrite	Clay	TOC (%)	Ro (%)	Tmax (°C)	S <sub>1</sub> (mg/g)	S <sub>2</sub> (mg/g)	HI (mg/g)
1	CL-1	S-101	2392.66	OPS	37.6	23.4			39	0.9704	1.68	492	0.56	2.12	218
2	CL-2	S-101	2397.93	OPS	33	15.0			52	0.8516	1.75	495	0.2	2.11	247
3	CL-3	S-101	2450.64	OPS	56.9		1.7		41.4	0.9204	1.96	507	1.26	2.24	243
4	CL-4	S-101	2463.65	OMSS	31	22.0			47	1.378	2.44	534	0.61	2.08	150
5	CL-5	S-101	2465.24	OMMS	0	48.0	19		30	1.516	1.97	507	0.02	0.04	3
6	CL-6	SL-2	3077.12	OMSS	41	19.0			40	1.122	1.95	506	0.22	0.54	48
7	CL-7	SL-2	3077.77	OPS	41.5	4.8			53.7	0.9264	1.99	508	0.14	0.44	47
8	CL-8	SL-2	3430.14	ORAS	34.4	10.1			50.5	3.569	1.98	508	0.11	0.66	18
9	CL-9	SL-2	3432.44	OMAS	30.6				69.4	1.516	1.35	473	0.16	0.26	17
10	CL-10	SL-2	3433.48	OMAS	36	0.5	0.9		62.6	1.395	1.43	478	0.1	0.35	25
11	CL-11	SL-2	3433.88	ORAS	37.4	6.6	0.8		55.2	2.519	1.64	489	0.12	0.36	14
12	CL-12	SL-2	3435.15	OMAS	35.5	6.2		2.8	55.5	1.186	1.68	491	0.34	0.31	26
13	CL-13	SL-2	3434.58	OMAS	42.4	6.1			51.5	1.791	1.67	491	0.09	0.27	23
14	CL-14	B-201	3742.5	OPS	52.2	16.7			31.1	0.8402	1.88	502	0.19	0.25	13
15	CL-15	B-201	3748.55	ORAS	36.8	6.4		1.6	55.2	3.533	1.90	503	0.87	1.29	154
16	CL-16	B-201	3893.93	OMAS	29.4	4.2	1.9		64.5	1.041	2.06	512	0.13	0.42	12
17	CL-17	B-201	3896.08	OMAS	30.1	2.3			67.6	1.084	2.09	514	0.35	0.51	47
18	CL-18	B-201	3897.67	OMAS	27.1	2.5	1.7		68.7	1.505	1.99	509	0.33	0.73	49
19	CL-19	B-201	3937.69	OMMS	40.4	4.9	6.3		46.1	1.597	2.06	512	0.41	0.78	49
20	CL-20	B-201	3938.2	ORSS	49.7	4.2			46.1	2.159	2.06	513	0.61	0.99	46
21	CL-21	B-201	3942.08	OPS	20.9			25.2	53.9	0.9213	2.08	513	0.07	0.1	11
22	CL-22	B-201	3943.27	ORMS	32.7	12	7.8		42.6	2.852	2.04	511	0.15	0.45	16

OPS: organic-poor shale; OMSS: organic-medium siliceous shale; OMMS: organic-medium mixed shale; ORAS: organic-medium argillaceous shale; OMAS: organic-medium argillaceous shale.

### 3. Results

#### 3.1. Organic Geochemistry and Mineralogy

The organic geochemistry and mineralogy composition of the Shahezi shale samples are presented in Table 1. The TOC contents are in the range of 0.8402–3.569 wt.%, with an average value of 1.599 wt.%. The Rock-Eval pyrolysis parameter  $S_1$  values are ranging from 0.02 to 1.26 mg of hydrocarbon (HC)/g of rock, with an average of 0.32 mg of HC/g of rock. The  $S_2$  values are in the range of 0.04–2.24 mg of HC/g of rock, and  $S_2$  for most samples is less than 1 mg of HC/g of rock.  $T_{max}$  values of the samples are larger than 473 °C, with the highest value up to 534 °C. The average hydrogen index (HI) is 67.1 mg of HC/g of TOC (3–247 mg/g). The dominant kerogen type is type III according to the cross-plots of  $T_{max}$  versus HI and  $S_2$  versus TOC (Figure 2). The vitrinite reflectance (Ro) values converted from the  $T_{max}$  values of the shale samples range between 1.34% and 2.4%, suggesting the maturity of dry gas stage.

Clay minerals are dominant in the Shahezi shales, with an average content over 50 wt.% (27.6–69 wt.%). Quartz contents vary from 20.9 to 56.9 wt.%, carbonate minerals vary from 2.3 to 15 wt.%, and feldspar are between 2.3 wt.% and 15 wt.% in the Shahezi shales. Trace amount of pyrite were detected, no more than 2.8 wt.% (Table 1).

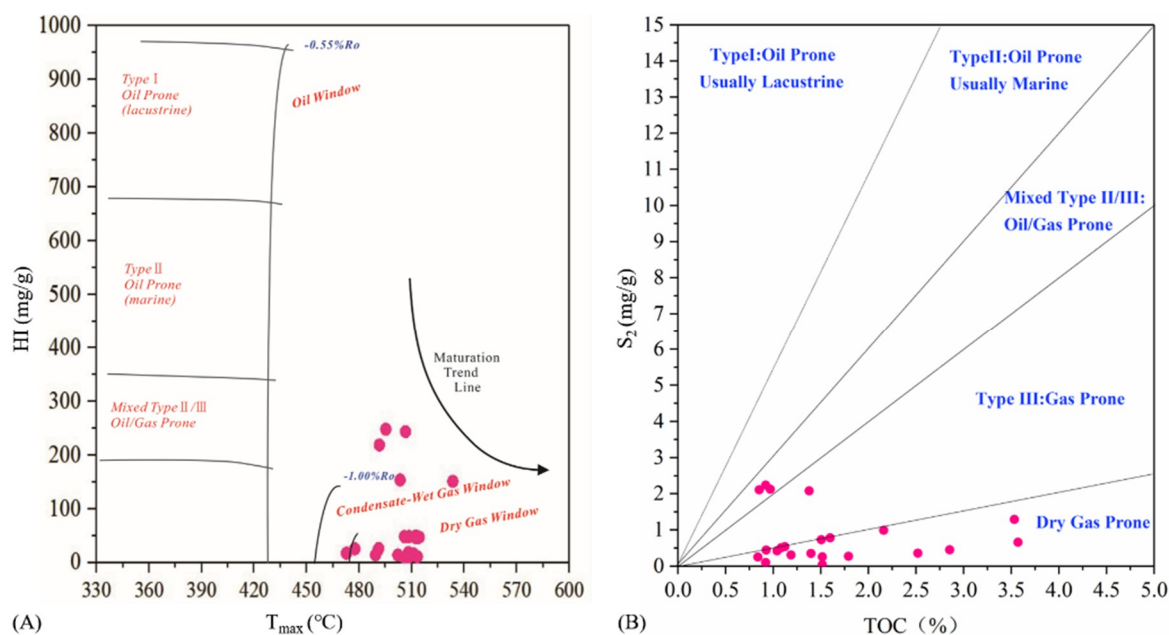


**Figure 2.** Cross-plots of  $T_{max}$  versus hydrogen index (A) and  $S_2$  versus total organic carbon (B) for identifying the kerogen type of the Shahezi shale in CFD.

#### 3.2. Lithofacies Classification

Shale lithofacies of the lacustrine Shahezi shales were sorted based on TOC and mineral compositions. Based on the classification scheme proposed by Gao et al. (2018) [30], seven shale lithofacies can be identified for the lacustrine shales in the CFD (Figure 3), including the organic-rich argillaceous shale (ORAS), organic-rich siliceous shale (ORSS), organic-rich mixed shale (ORMS), organic-medium argillaceous shale (OMAS), organic-medium siliceous shale (OMSS), organic-medium mixed shale (OMMS), and organic-poor shale (OPS). Since shales with TOC content less than 1 wt.% were not considered as target layers [14,27], they are summed together as organic poor shale (OPS).

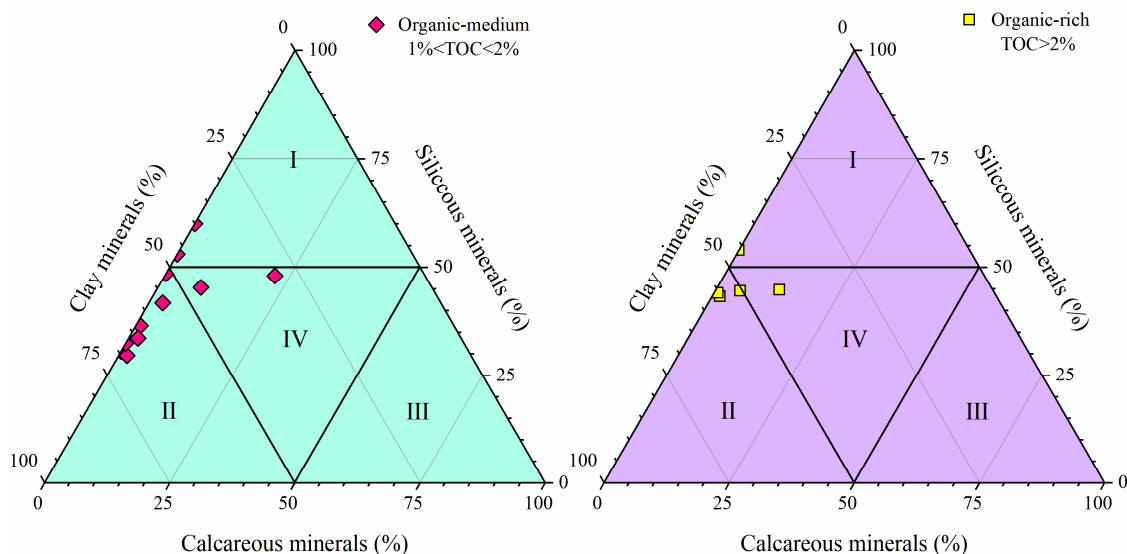


**Figure 3.** Lithofacies classification of the Shahezi shales in CFD (I: siliceous shale; II: argillaceous shale; III: calcareous shale; IV: mixed shale).

### 3.3. Field Emission-Scanning Electron Microscope (FE-SEM) Imaging

#### 3.3.1. Organic Matter Pores

As seen from the FE-SEM images, few organic matter (OM) pores were observed in the Shahezi shale samples (Figure 4). Pyrite framboids filled by OM were commonly seen (Figure 4A) with small oval pores (around 30 nm) (Figure 4B). Heterogeneous distribution of OM pores with larger pores in the center and no pores in the rim of the same OM particle were observed (Figure 4C). OM coexist with clay and siliceous minerals host complex pore networks. Sponge-like shaped pores with pore size over 300 nm are generated in OM coexisted with quartz (Figure 4D,E). The OM may also be mixed with clay minerals forming organic-clay composites, which have relatively abundant OM pores (Figure 4F). Larger pores contain smaller sponge-like pores, forming complex pore networks in three dimensions, which may have better connectivity within the OM (Figure 4G–I). The sponge-like pores were also observed where OM coexists with pyrite framboids (Figure 4J,K). Same samples have completely different pore characteristics (Figure 4C,L). The same observations were reported in Woodford shale samples with a measured  $R_o$  value of 1.4%, which may be due to organic macerals heterogeneity or OM difference (non-porous kerogen/porous pyrobitumen) [38].

#### 3.3.2. Inorganic Minerals Pores

Inorganic pores, mainly hosted in clay minerals, feldspar and quartz, are abundant in the Shahezi shales in CFD (Figure 5). Frequently observed pores are slit-like intraparticle pores (intraP pores) and interparticle pores (interP pores) within clay mineral composites (Figure 5A–F). Many Linear pores between clay platelets were found in the pressure shadow of the rigid minerals (Figure 5A,B). Intraparticle pores were also observed within the mixed illite-smectite and chlorite aggregates (Figure 5C,D). Many interP pores within clay minerals are filled with pyrite particles (Figure 5E). Micro-fractures are easily formed in the clay aggregates (Figure 5F). Oval intraP pores in siliceous and calcareous minerals are observed (Figure 5G–L). InterP pores of quartz and calcite are also observed with a shape of triangular or polygonal (Figure 5K,L). These pores are probably originated from organic acid dissolution [1].

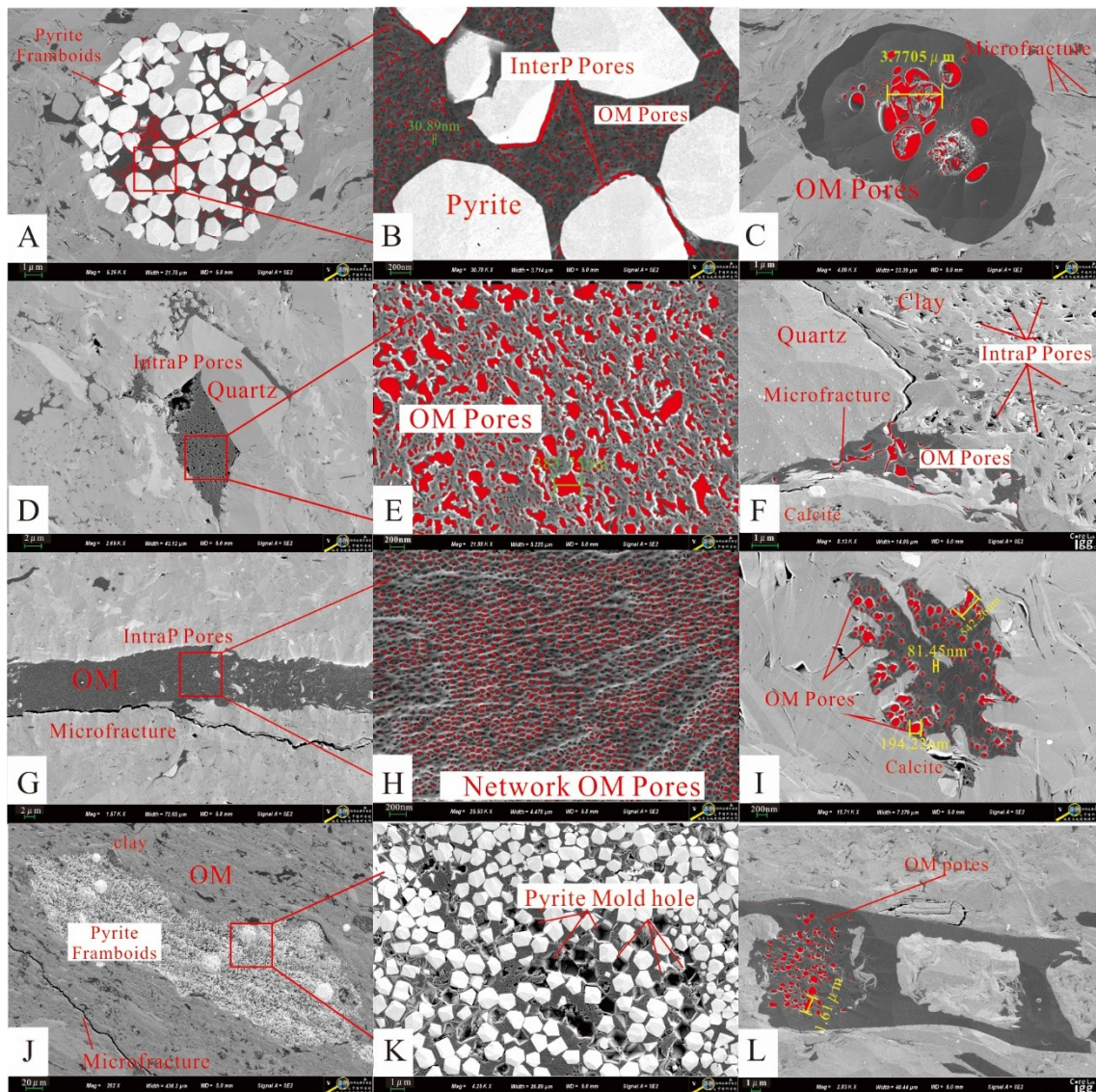


**Figure 4.** FE-SEM images of OM pores in the Shahezi shales in CFD. (A) OM filled in pyrite framboids grains contain small oval OM pores with pore diameters of about 30 nm. (B) enlarged square area from image A. (C) Heterogeneous characteristics of organic matter (OM) pores. (D,E) Sponge-like OM pores hosted in OM coexist with quartz. (F) cracks around quartz grains and pores in OM-clay composites. (G,H) Complex OM pore networks with small width. (I) Heterogeneous OM pore characteristics in the same OM particle with wide pore size. (J,K) mold holes and OM pores associated with pyrite framboids. (L) Different pore characteristics in same samples.

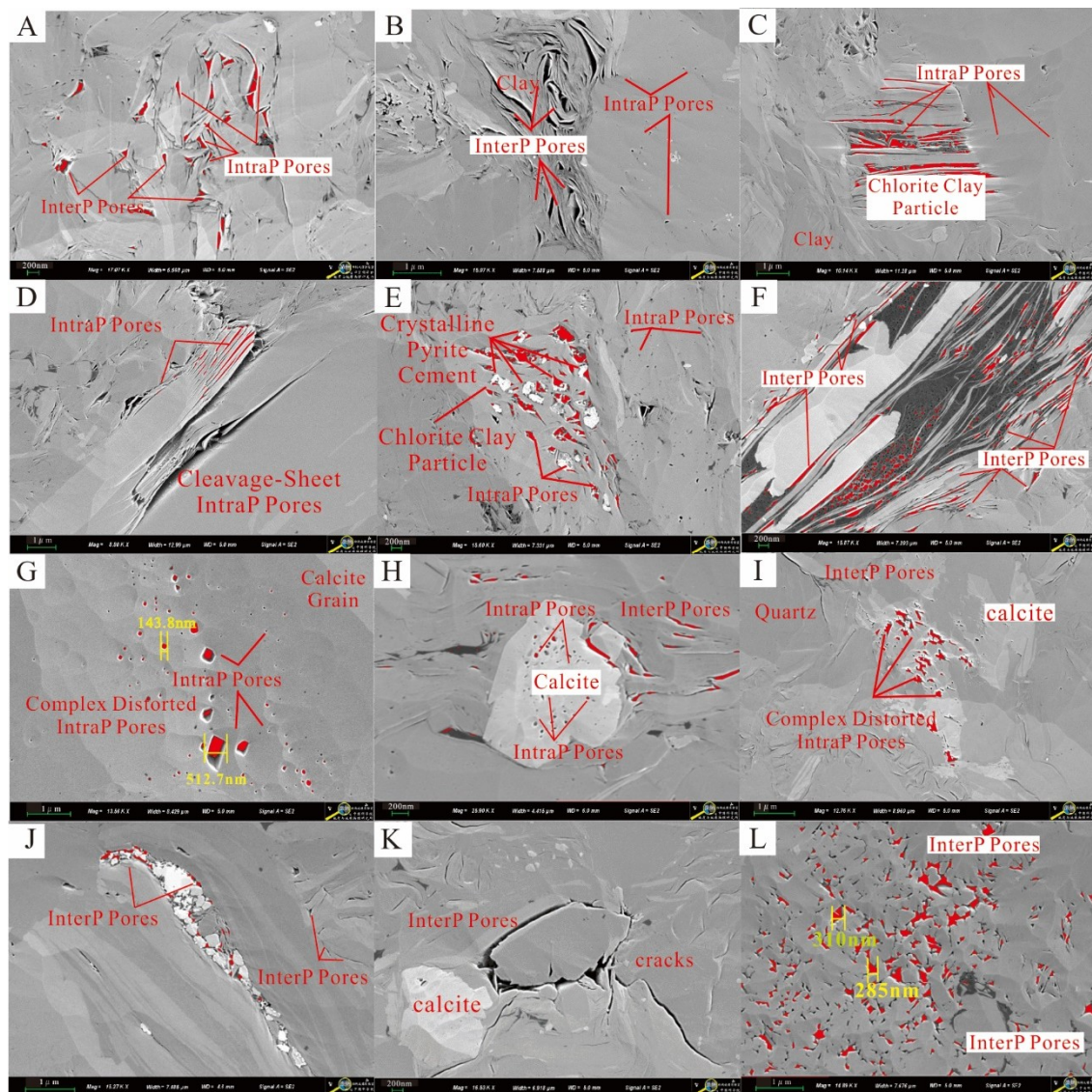


**Figure 5.** FE-SEM images showing inorganic mineral pores in the Shahezi shales in CFD. (A–F) Slit-like interP pores and intraP pores in clay composites. (G–I) IntraP pores hosted in siliceous and calcareous minerals. (J) InterP pores are filled with pyrite framboids. (K) Micro-cracks developed at the edge of inorganic mineral grains. (L) Complex intergranular pores between quartz grains.

### 3.3.3. Image Processing Analyses

Shales display strong heterogeneity at the micro scale and becomes weaker heterogeneity in a larger field of view, therefore, representative elementary area (REA) were taken at a magnification of  $\times 20,000$  [39]. REA images of the Shahezi shales were quantitatively studied using Image-Pro Plus software [40]. The parameters of pores image processing, including pore width, length, perimeter, area and fractal dimension, are listed in Table 2. Totally 3669 pores, including OM pores, interP pores and intraP pores, were extracted from the REA images of the Shahezi shales. InterP pores contribute the highest percentage in the total pore systems (58.8%). However, intraP pores contribute the lowest percentage (5.6%). The mean pore sizes of the OM pores, interP pores, and intraP pores are 35.6, 56.2, and 27.9 nm. IntraP pores have the lowest fractal dimension (1.06), while the interP pores have the highest value (1.44) among the three pore types. These fractal dimension data reveal that the intraP pores have the most regularly shaped pores, while the interP pores are the most irregularly shape in the Shahezi shales in CFD.

**Table 2.** Image processing results of representative elementary area (REA) for the Shahezi shale in CFD.

Pore Type	Number of Pores	Percentage (%)	Pore Size (nm)			Pore Area (nm <sup>2</sup> )	Fractal Dimension
			Min Value	Max Value	Mean		
OM pore	1306	35.6	12.6	355.9	35.6	4996.2	1.18
InterP pore	2157	58.8	18.8	890.6	56.2	8762.3	1.44
IntraP pore	206	5.6	25.9	240.4	27.9	2237.8	1.06

**3.4. LPNP Isotherms and FHH Fractal Dimensions**

The LPNP isotherms of the selected lacustrine shale samples are plotted in terms of shale lithofacies (Figure 6). The hysteresis loops show H3 and H4 shapes according to the classification of IUPAC [41,42], indicating slit-like and ink-bottle pores exist in the Shahezi shales. The organic-rich shales (TOC > 2 wt.%) have relatively higher adsorption volumes than organic lean shales (TOC < 2 wt.%). Among the shale lithofacies, the decreasing order of adsorption capacity is: OMMS > OMAS > ORAS > ORMS > ORSS > OMSS > OPS.

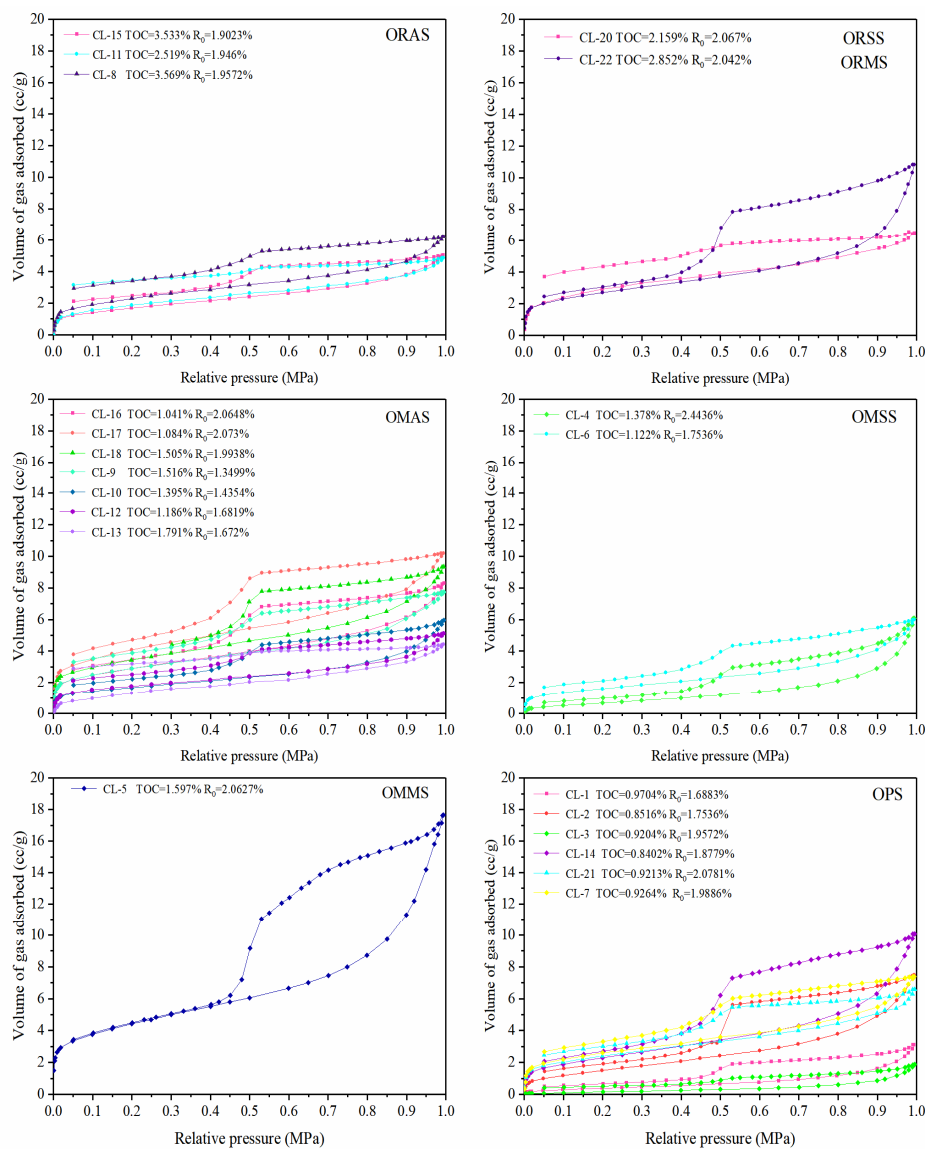


**Figure 6.** Low pressure nitrogen physisorption (LPNP) isotherms of the Shahezi shales with different lithofacies in CFD.

The FHH plots of the Shahezi shales are shown in Figure 7. Two linear segments in the relative pressure ( $P/P_0$ ) ranges of 0–0.5 and 0.5–1 were identified. The fitting equations, correlation coefficients and calculated fractal dimensions ( $D_1$  and  $D_2$ ) are summarized in Table 3. The fractal dimension  $D_1$  values are relatively low, ranging from 2.0336 to 2.5957, with a mean value of 2.4385. The fractal dimension  $D_2$  values are in the range of 2.5779–2.8821, with an average of 2.7703, indicating high pore structure complexity in larger pores [9,15,23].

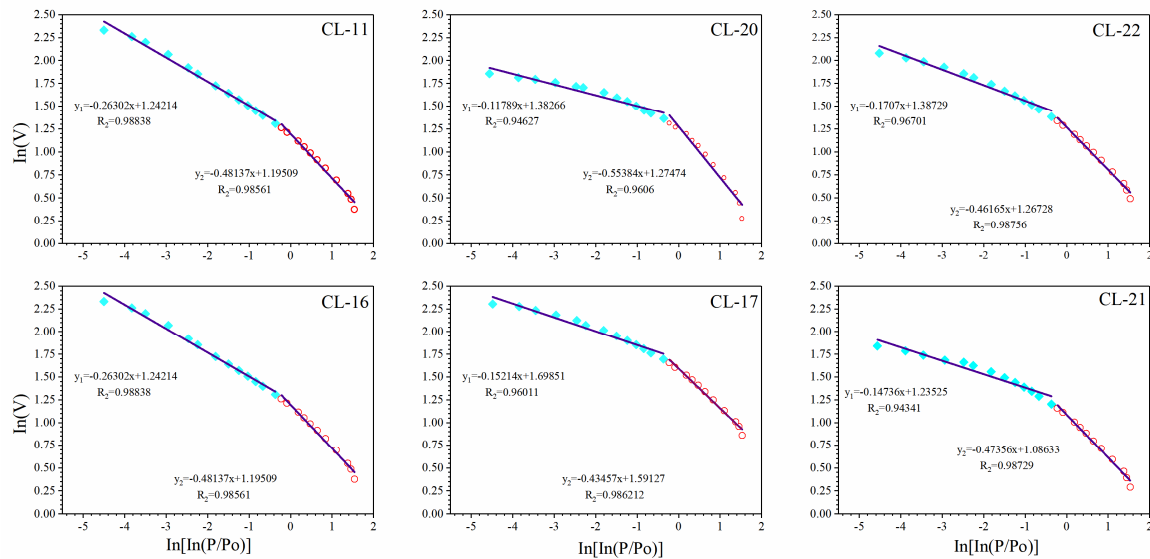


**Figure 7.** Plots of  $\ln V$  versus  $\ln(\ln P_0/P)$  obtained from the adsorption branch of LPNP isotherms of the Shahezi shales with different lithofacies in CFD.

### 3.5. MICP Analysis

The results of MICP are summarized in terms of lithofacies (Figure 8). The cumulative mercury intrusion volumes for each sample are similar. The curves show a rapid increase of mercury intrusion volume to a certain value at low pressures, suggesting cracks may generate during sample preparation process [43]. In the pressure range of 10–10,000 Psi, the cumulative intrusion volumes increase slowly (Figure 8). When intrusion pressure exceeds 10,000 Psi, the intrusion volumes increases rapidly to the maximum values. In the stage of pressure decreases, no obvious variation can be identified in the pressure range of 100–30,000 Psi and extrusion volumes decrease in the pressure range of 1–20 Psi. The variation trends of the MICP curves suggest shales have abundant nanoscale pores with bottle-necked shapes and poor pore connectivity [10,43,44].

**Table 3.** Fractal dimensions obtained from the Frenkel–Halsey–Hill (FHH) model using LPNP isotherms.

Sample ID	Lithofacies	Fitting Equation	$k_1$	$D_1$	Coefficient ( $R^2$ )	Fitting Equation	$k_2$	$D_2$	Coefficient ( $R^2$ )
CL-14	OPS	$y = -0.5988x + 1.0935$	-0.5988	2.4012	0.9713	$y = -0.2698x + 1.1944$	-0.3	2.7302	0.9751
CL-15	ORAS	$y = -0.5406x + 0.7522$	-0.5406	2.4594	0.9817	$y = -0.1774x + 0.8864$	-0.2	2.8226	0.9599
CL-16	OMAS	$y = -0.4616x + 1.2673$	-0.4616	2.5384	0.9888	$y = -0.1707x + 1.3873$	-0.2	2.8293	0.967
CL-17	OMAS	$y = -0.4346x + 1.5913$	-0.4346	2.5654	0.9876	$y = -0.1521x + 1.6985$	-0.2	2.8479	0.9634
CL-18	OMAS	$y = -0.4043x + 1.4172$	-0.4043	2.5957	0.996	$y = -0.1671x + 1.5363$	-0.2	2.8329	0.9618
CL-19	OMMS	$y = -0.4346x + 1.5913$	-0.4346	2.5654	0.9876	$y = -0.1521x + 1.6985$	-0.2	2.8479	0.9634
CL-20	ORSS	$y = -0.5538x + 1.2747$	-0.5538	2.4462	0.9607	$y = -0.1179x + 1.3827$	-0.1	2.8821	0.9363
CL-21	OPS	$y = -0.4736x + 1.0863$	-0.4736	2.5264	0.9886	$y = -0.1474x + 1.2352$	-0.1	2.8526	0.9434
CL-22	ORMS	$y = -0.4814x + 1.1951$	-0.4814	2.5186	0.987	$y = -0.263x + 1.2421$	-0.3	2.737	0.9896
CL-6	OMSS	$y = -0.5332x + 0.711$	-0.5332	2.4668	0.9881	$y = -0.2223x + 0.8492$	-0.2	2.7777	0.9653
CL-7	OPS	$y = -0.4814x + 1.1951$	-0.4814	2.5186	0.987	$y = -0.263x + 1.2421$	-0.3	2.737	0.9894
CL-8	ORAS	$y = -0.4648x + 1.0287$	-0.4648	2.5352	0.993	$y = -0.1601x + 1.1526$	-0.2	2.8399	0.9703
CL-9	OMAS	$y = -0.4508x + 1.2572$	-0.4508	2.5492	0.985	$y = -0.1715x + 1.3519$	-0.2	2.8285	0.9571
CL-10	OMAS	$y = -0.4393x + 0.7203$	-0.4393	2.5607	0.9966	$y = -0.2436x + 0.8057$	-0.2	2.7564	0.9869
CL-11	ORAS	$y = -0.4814x + 1.1951$	-0.4814	2.5186	0.987	$y = -0.263x + 1.2421$	-0.3	2.737	0.9894
CL-12	OMAS	$y = -0.5027x + 0.7836$	-0.5027	2.4973	0.9576	$y = -0.1785x + 0.867$	-0.2	2.8215	0.9763
CL-13	OMAS	$y = -0.842x + 0.5915$	-0.842	2.158	0.9415	$y = -0.1831x + 0.7362$	-0.2	2.8169	0.9388
CL-1	OPS	$y = -0.7984x - 0.5986$	-0.7984	2.2016	0.9905	$y = -0.3638x - 0.4258$	-0.4	2.6362	0.9701
CL-3	OPS	$y = -0.9664x - 1.4317$	-0.9664	2.0336	0.9967	$y = -0.4221x - 1.183$	-0.4	2.5779	0.9696
CL-4	OMSS	$y = -0.7577x - 0.05$	-0.757	2.243	0.9984	$y = -0.3871x + 0.1337$	-0.4	2.6129	0.9824
CL-5	OMMS	$y = -0.4417x + 1.6823$	-0.4417	2.5583	0.9965	$y = -0.2737x + 1.7491$	-0.3	2.7263	0.9698
CL-2	OPS	$y = -0.6771x + 0.7099$	-0.6771	2.3229	0.9921	$y = -0.4417x + 1.6824$	-0.3	2.7264	0.9595

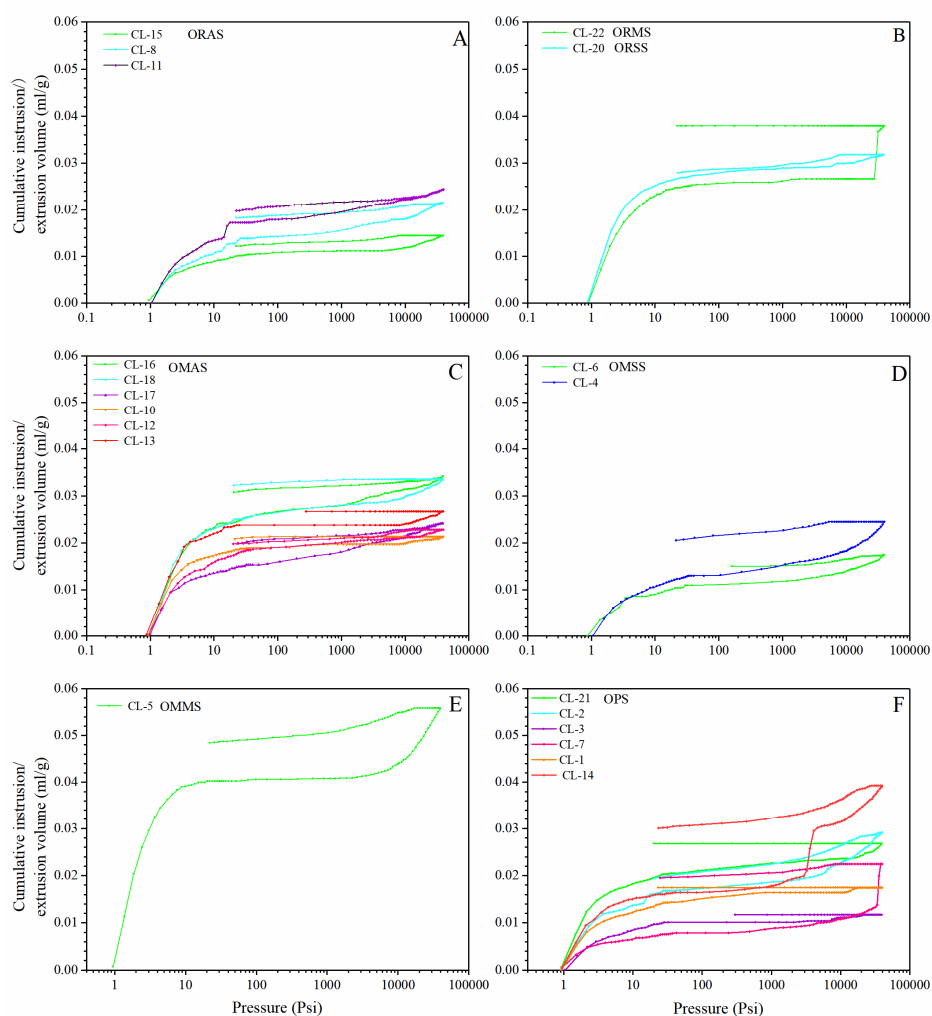


**Figure 8.** Mercury intrusion capillary pressure (MICP) intrusion and extrusion volumes for the Shahezi shales with different lithofacies in CFD.

### 3.6. Full-Size Pore Characterization

The full-size pore size distribution (PSD) characteristics of the selected shale samples are obtained by combining LPNP and MICP data (Figure 9). The method was proposed and effectively used for characterization of pore characteristics in organic shales [10,45,46]. The results show that multimodal characteristics were shown in the PSD spectra in 0.5–0.9 nm, 3–6 nm and 10–40 nm (Figure 9). The PSD characteristics vary in different lithofacies. The OMMS has the highest total pore volumes of 0.0328 mL/g, followed by the ORMS. The proportions of micropores, mesopores and macropores for the Shahezi shale samples are shown in Figure 10. The characteristics of nanopore systems show greater variation with the increasing buried depth. The mesopores primarily contribute to the pore volumes of the Shahezi shales. Mesopores and macropores account for 66.0%–88.3% of the total pore volume (Table 4).

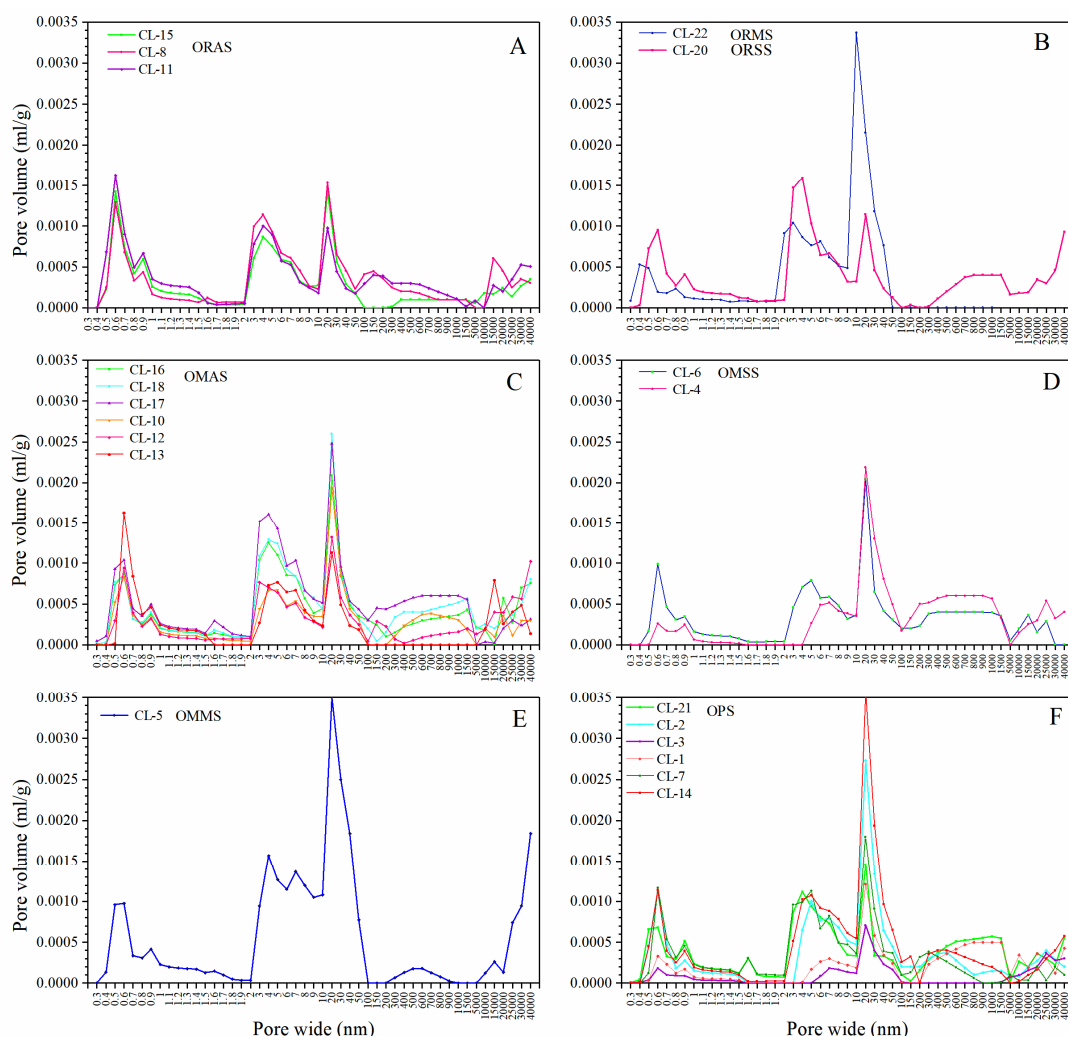


**Figure 9.** Full-size pore size distribution (PSD) characteristics of pore volumes of the Shahezi shales with different lithofacies in CFD.

**Table 4.** Pore structure parameters of lacustrine shale samples with different lithofacies in CFD.

Sample ID	Lithofacies	Pore Volume (cm <sup>3</sup> /g)				Percentage (%)		
		Micropore	Mesopore	Macropore	Total	Micropore	Mesopore	Macropore
CL-15	ORAS	0.0045	0.0055	0.0022	0.0122	36.80	45.13	18.07
CL-8		0.0036	0.0058	0.0067	0.0162	22.47	36.07	41.46
CL-11		0.0044	0.0026	0.0079	0.0149	29.70	17.37	52.93
Mean		0.0042	0.0046	0.0056	0.0144	29.00	32.17	38.84
CL-20	ORSS	0.0039	0.0043	0.0042	0.0123	31.28	34.68	34.04
Mean		0.0039	0.0043	0.0042	0.0123	31.28	34.68	34.04
CL-22	ORMS	0.0023	0.0175	0.0065	0.0263	8.80	66.46	24.75
Mean		0.0023	0.0175	0.0065	0.0263	8.80	66.46	24.75
CL-16	OMAS	0.0035	0.0103	0.0071	0.0209	16.79	49.22	33.99
CL-17		0.0046	0.0122	0.0067	0.0235	19.63	51.88	28.48
CL-9		0.0041	0.0083	0.0068	0.0193	21.48	43.22	35.30
CL-10		0.0030	0.0078	0.0024	0.0132	22.77	59.03	18.20
CL-12		0.0027	0.0053	0.0036	0.0116	23.37	45.55	31.07
CL-13		0.0044	0.0023	0.0019	0.0086	51.38	26.59	22.03
Mean		0.0037	0.0083	0.0049	0.0169	22.06	48.96	28.98

Table 4. Cont.

Sample ID	Lithofacies	Pore Volume (cm <sup>3</sup> /g)				Percentage (%)		
		Micropore	Mesopore	Macropore	Total	Micropore	Mesopore	Macropore
CL-6	OMSS	0.0030	0.0080	0.0039	0.0149	19.93	53.88	26.20
Mean		0.0030	0.0080	0.0039	0.0149	19.93	53.88	26.20
CL-5	OMMS	0.0042	0.0186	0.0125	0.0353	11.92	52.69	35.41
CL-19		0.0036	0.0116	0.0057	0.0209	17.31	55.46	27.23
Mean		0.0039	0.0151	0.0091	0.0281	14.615	54.075	31.32
CL-1	OPS	0.0012	0.0048	0.0042	0.0102	11.72	47.10	41.18
CL-3		0.0007	0.0025	0.0020	0.0052	13.62	47.65	38.72
CL-7		0.0036	0.0087	0.0032	0.0155	23.35	56.01	20.64
CL-21		0.0036	0.0073	0.0050	0.0159	22.48	46.12	31.39
Mean		0.0026	0.0062	0.0034	0.0122	21.60	50.53	27.87

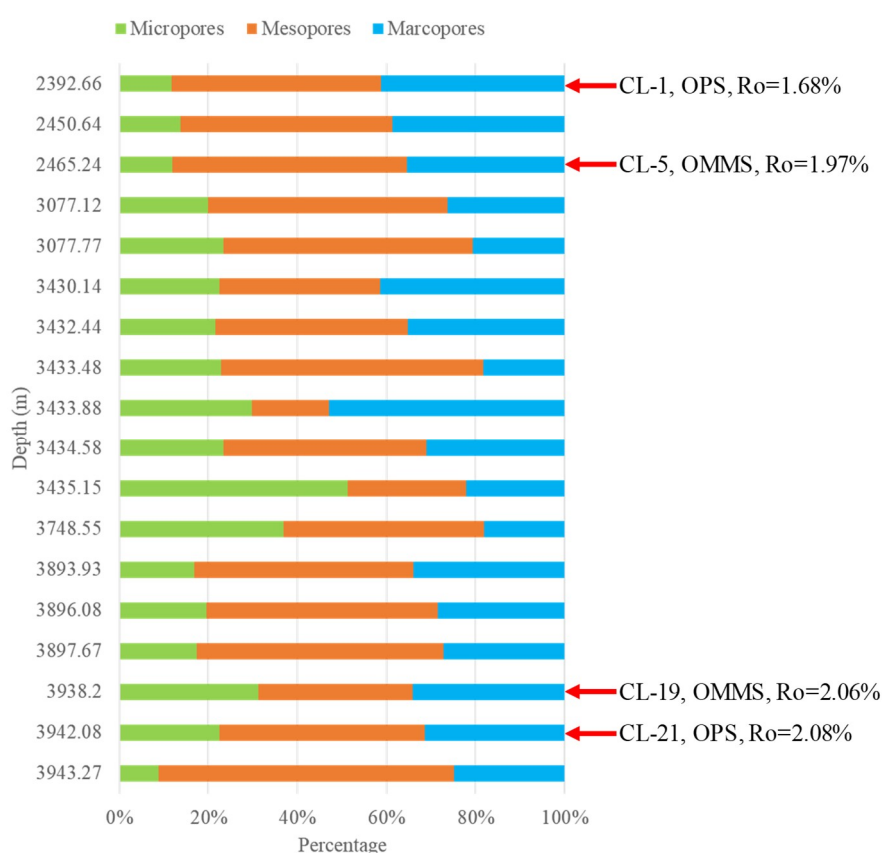


Figure 10. Percentage of pore volumes of the Shahezi shales along with depth in CFD.

#### 4. Discussion

The development of pore structure is the combined effect of multiple factors, including TOC, thermal evolution (burial depth), and mineral composition [1,47,48]. Seven shale lithofacies can be identified for the lacustrine shales in CFD (Figure 3). These lithofacies display variable proportions of quartz, clay, and carbonate. Therefore, the impacts of lithofacies on pore structure and fractal dimensions are discussed in terms of OM richness and mineral compositions.

#### 4.1. The Impacts of Lithofacies on Pore Structure

The ORSS and ORMS with similar TOC, clay mineral and quartz content, vary significantly in pore volumes, which may be caused by different calcite contents with dissolved pores ORMS (Figure 4G–I). Compared with ORAS, the OMAS has larger pore volumes, suggesting the contribution of clay minerals to pore volumes is greater than that of organic matter (Figure 4). The pore volumes of the OPS samples show a large variation. Due to the low TOC content, the mineral composition has a great influence on the pore structure, such as CL-2 and CL-7 clay content are more than 50%.

No obvious correlation between the burial depth and pore percentage were observed in Figure 10. Therefore, burial depth may not independently control the pore size distribution and porosity of shales [41]. By compare the pore volumes of shale samples with similar lithofacies and different burial depth, the possible impacts of burial depth on macro-, meso-, and micropore volumes were discussed. The decline in macropore and mesopore volumes in deeply buried shales samples (CL-19 and CL-21) is probably the results of deepen burial (Figure 10). Larger pores from shales buried over 3500 m may be compacted and greatly decrease the pore size and total pore volumes [41].

The correlations between micropore, mesopore and macropore volumes and TOC are plotted in Figure 11A–C. The micropore and mesopore volumes show slightly positive correlations with TOC contents, suggests the contribution of OM pores to the total pore networks in the Shahezi shale may not be dominant. The TOC contents of in the Shahezi shale is much lower (0.92%–3.57%, averaging 1.69%) than that of the Barnett (3%–13%, averaging 4.5%) and Longmaxi shales (0.87%–8.01%, averaging 3.44%) [12,49–51], which may be insufficient to provide significant pores [48,51]. The heterogeneity of organic pore distribution may be another reason for the weak correlation between pore volumes and TOC contents, which is related to the maceral types of OM [38,50] (Figure 4C,L). Negative correlations of micropores, mesopores, and macropores with quartz are presented in Figure 11D–F. The Shahezi shales are deeply buried (Table 1), therefore, under the effect of compaction, the primary pores between brittle grains gradually shrink and even disappear [52], indicating the siliceous minerals generally have a limited effect on the pore development. With the increase of clay mineral content, the pore volumes of micropores, mesopores and macropores all increase, indicating the various development of clay related pores in different pore size ranges (Figure 11G–I and Table 4). Clay minerals are dominant in the Shahezi samples, which are often associated with OM and quartz (Figure 5). In addition, previous study from study area reveal that clay minerals commonly host abundant clay related pores in the Shahezi shales, which have a much larger pore volume than other minerals [34]. During the transformation of montmorillonite to illite or chlorite, an increase trend in the number of micropores and mesopores appears [34,53,54]. Therefore, clay minerals are the essential controlling factor of pore development in the Shahezi shales in CFD. No obvious correlation was observed between multiscale pore volumes and carbonate components (Figure 11J–L). IntraP pores can be formed due to the solubility of calcite, consequently, abundant calcite contents may play significant roles in pore development in organic shales [7,47,55]. Relatively small amount of calcite and dolomite with dissolved pores are identified in the Shahezi shales, which may be the cause of the scatter correlations in the plots of pore volumes against carbonate contents.

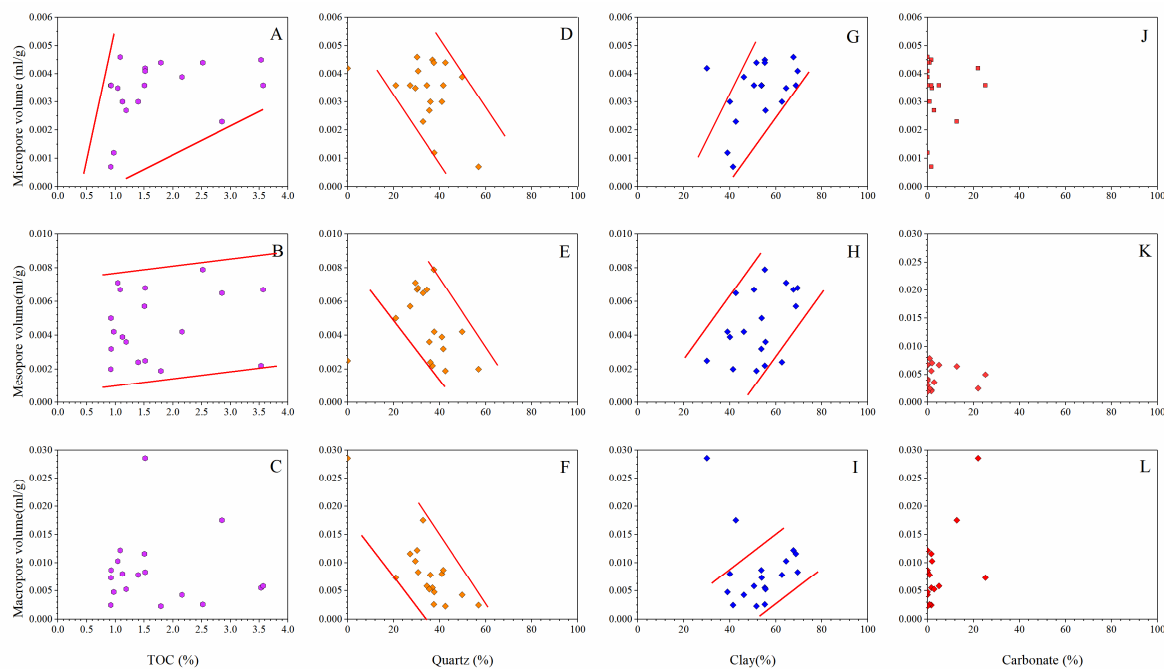


**Figure 11.** Relationships between pore structure parameters and TOC, mineral compositions: (A) Micropore volume versus TOC content; (B) Mesopore volume versus TOC content; (C) Macropore volume versus TOC content; (D) Micropore volume versus quartz content; (E) Mesopore volume versus quartz content; (F) Macropore volume versus quartz content; (G) Micropore volume versus clay mineral content; (H) Mesopore volume versus clay mineral content; (I) Macropore volume versus clay mineral content; (J) Micropore volume versus carbonate mineral content; (K) Mesopore volume versus carbonate mineral content; (L) Macropore volume versus carbonate mineral content.

#### 4.2. The Impacts of Lithofacies on Pore Fractal Dimensions

The impacts of mineralogy-based lithofacies on nanopore fractal dimensions were discussed in aspects of matrix composition, including TOC, quartz, clay, and calcareous mineral contents. The different proportions of mineral components in the seven lithofacies strongly affect the fractal dimensions in the Shahezi shales. The OMAS has the highest  $D_1$ , probably because of the highest clay content in these shales (Table 3). OPS have the lowest  $D_1$  and  $D_2$ , which may be caused by the much lower TOC and clay contents than the other lithofacies (Table 3).

The relationships between the fractal dimensions ( $D_1$ ,  $D_2$ ) and rock compositions including TOC, clay minerals, quartz, and carbonates are presented in Figure 12. Fractal dimensions show slightly positive correlations with TOC contents (Figure 11A,B). This result is probably due to the relatively low organic richness and insufficient OM pores in the Shahezi shales, and is inconsistent with the fractal dimensions of the over-mature marine shales [9,15,22]. OM pores with smaller pore width may result in more complex pore networks in organic shales [1,8,12], consequently, increase the fractal dimensions  $D_1$  and  $D_2$ . In FE-SEM images, few OM pores were observed in the selected lacustrine shales (Figure 4), which may explain the weak correlations of fractal dimensions with TOC content [22].

With the increase of clay contents, both the  $D_1$  and  $D_2$  values increase (Figure 12E,F). Clay minerals are the main components in lacustrine shales of the Shahezi Formation, with an average content over 50% (Table 1). In addition, OM are commonly associated with clay minerals forming complex OM-clay composites (Figure 5A–F). As clay minerals host abundant complex interP and intraP pores, which may enhance the heterogeneity of pore volumes, result in larger fractal dimensions [10,15,22]. The relationships between fractal dimensions and quartz contents display negative correlations (Figure 12C,D) and no obvious correlations of fractal dimensions with calcareous minerals were observed (Figure 12G,H). The slight negative linear relationship between fractal dimension  $D_1$  and

brittle minerals (quartz and carbonate) contents, indicating the brittle minerals have a little effect on fractal dimension  $D_1$ . This is possibly because the more homogenous nature of pore volumes than organic matter and clay minerals. Fractal dimension  $D_2$  decreases with increasing brittle minerals. This result is probably due to the relatively small amount of calcite and dolomite with dissolved pores shown in the FE-SEM images of the Shahezi shales (Figure 5H,I,L) and the better protection of complex organic pore network from numerous brittle mineral grains (Figure 4), L), which results in a greater fractal dimension  $D_2$  [22].

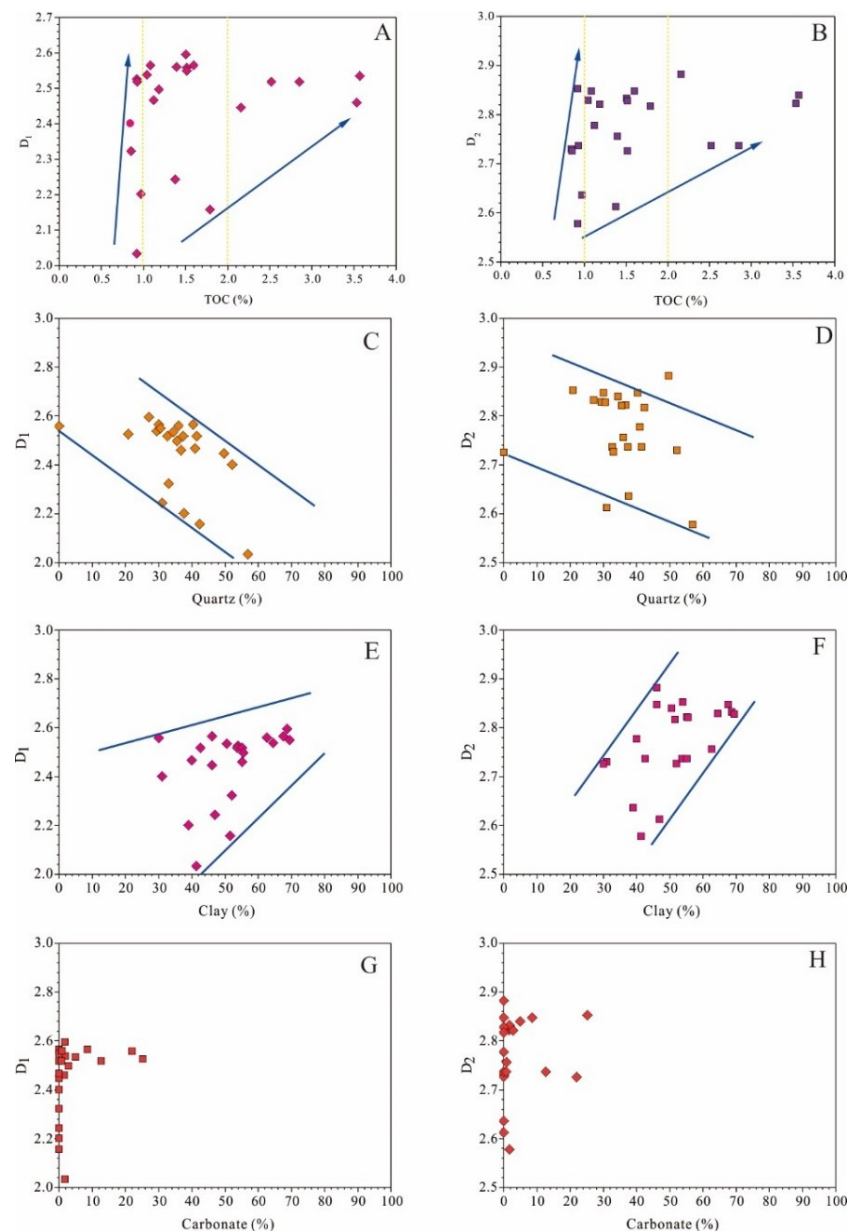


**Figure 12.** Relationship between fractal dimensions ( $D_1$ ,  $D_2$ ) and OM and inorganic mineral compositions: (A)  $D_1$  versus TOC content; (B)  $D_2$  versus TOC content; (C)  $D_1$  versus quartz content; (D)  $D_2$  versus quartz content; (E)  $D_1$  versus clay mineral content; (F)  $D_2$  versus clay mineral content; (G)  $D_1$  versus carbonate mineral content; (H)  $D_2$  versus carbonate mineral content.

## 5. Conclusions

Based on our studies, the following conclusions can be drawn.

(1) Seven lithofacies, including the organic-rich argillaceous shale (ORAS), organic-rich siliceous shale (ORSS), organic-rich mixed shale (ORMS), organic-medium argillaceous shale (OMAS), organic-medium siliceous shale (OMSS), organic-medium mixed shale (OMMS), and organic-poor shale (OPS), are identified and sorted based on a mineralogy-based classification scheme for the lacustrine shales in the CFD.

(2) Two fractal dimensions,  $D_1$  and  $D_2$ , were obtained at relative pressures of 0–0.5 and 0.5–1 using the FHH model. The  $D_1$  and  $D_2$  values are in range of 2.0336–2.5957 and 2.5779–2.8821, respectively.  $D_2$  values are slightly greater than  $D_1$ , indicating small pores may form more complex pore networks in the Shahezi shales.

(3) Fractal dimensions of the selected lacustrine shales are affected by shale mineral compositions and pore structure parameters. OMAS shale, rich in clay, have comparatively high fractal dimension  $D_1$ . ORAS shale, rich in TOC and clay, have comparatively high fractal dimension  $D_2$ . OPS shale, rich in siliceous and lack of TOC, have the lowest  $D_1$  and  $D_2$ .

(4) Pore structure and fractal dimensions, which are a combined function of organic and inorganic composition, varies among the shale lithofacies. Samples with higher clay content have larger pore width, whereas samples with low clay content have smaller pore width. clay contents are the most significant factor controlling the pore structure and fractal dimensions of the lacustrine Shahezi shale in CFD. Observations of few organic matter pores and abundant inorganic pores hosted in the Shahezi shales may contribute to these correlations.

**Author Contributions:** Z.L. (Zhuo Li) and Z.J. designed and supervised the project; F.G., Y.Z. and Z.L. (Zhikai Liang) performed the experiments and analyzed the data; Z.L. (Zhikai Liang) wrote this paper and Z.L. (Zhuo Li) corrected it; H.Y., L.X., and Y.Y. modified the formats.

**Funding:** This research was funded by National Science and Technology Major Project, grant number 2016ZX05034-001 and the National Natural Science Foundation of China, grant number 41502123 and the APC was funded by National Science and Technology Major Project, grant number 2016ZX05034-001.

**Acknowledgments:** The northeast Branch of SINOPEC, China is thanked for providing shale samples and geological background references. We are grateful to editors and reviewers for their constructive comments and suggestions.

**Conflicts of Interest:** The authors declare no conflict of interest.

## References

1. Loucks, R.G.; Reed, R.M.; Ruppel, S.C.; Hammes, U. Spectrum of pore types and networks in mudrocks and a descriptive classification for matrix-related mudrock pores. *AAPG Bull.* **2012**, *96*, 1071–1098. [[CrossRef](#)]
2. Clarkson, C.R.; Solano, N.; Bustin, R.M.; Bustin, A.M.M.; Chalmers, G.R.L.; He, L.; Melnichenko, Y.B.; Radlinski, A.P.; Blach, T.P. Pore structure characterization of North American shale gas reservoirs using USANS/SANS, gas adsorption, and mercury intrusion. *Fuel* **2013**, *103*, 606–616. [[CrossRef](#)]
3. Tang, X.L.; Jiang, Z.X.; Li, Z.; Gao, Z.Y.; Bai, Y.Q.; Zhao, S.; Feng, J. The effect of the variation in material composition on the heterogeneous pore structure of high-maturity shale of the Silurian Longmaxi formation in the southeastern Sichuan Basin, China. *J. Nat. Gas Sci. Eng.* **2015**, *23*, 464–473. [[CrossRef](#)]
4. Wang, P.F.; Jiang, Z.X.; Yin, L.S.; Chen, L.; Li, Z.; Zhang, C.; Li, T.W.; Huang, P. Lithofacies classification and its effect on pore structure of the Cambrian marine shale in the Upper Yangtze Platform, South China: Evidence from FE-SEM and gas adsorption analysis. *J. Pet. Sci Eng.* **2017**, *156*, 307–321. [[CrossRef](#)]
5. Loucks, R.G.; Reed, R.M.; Ruppel, S.C.; Jarvie, D.M. Morphology, Genesis, and Distribution of Nanometer-Scale Pores in Siliceous Mudstones of the Mississippian Barnett Shale. *J. Sediment. Res.* **2009**, *79*, 848–861. [[CrossRef](#)]
6. Chalmers, G.R.L.; Ross, D.J.K.; Bustin, R.M. Geological controls on matrix permeability of Devonian Gas Shales in the Horn River and Liard basins, northeastern British Columbia, Canada. *Int. J. Coal Geol.* **2012**, *103*, 120–131. [[CrossRef](#)]

7. Li, A.; Ding, W.L.; Wang, R.Y.; He, J.H.; Wang, X.H.; Sun, Y.X.; Gu, Y.; Jiao, N.L. Petrophysical characterization of shale reservoir based on nuclear magnetic resonance (NMR) experiment: A case study of Lower Cambrian Qiongzhusi Formation in eastern Yunnan Province, South China. *J. Nat. Gas Sci. Eng.* **2017**, *37*, 29–38. [[CrossRef](#)]
8. Ross, D.J.K.; Bustin, R.M. The importance of shale composition and pore structure upon gas storage potential of shale gas reservoirs. *Mar. Pet. Geol.* **2009**, *26*, 916–927. [[CrossRef](#)]
9. Yang, F.; Ning, Z.F.; Liu, H.Q. Fractal characteristics of shales from a shale gas reservoir in the Sichuan Basin, China. *Fuel* **2014**, *115*, 378–384. [[CrossRef](#)]
10. Wang, G.C.; Ju, Y.W.; Yan, Z.F.; Li, Q.G. Pore structure characteristics of coal-bearing shale using fluid invasion methods: A case study in the Huainan-Huaibei Coalfield in China. *Mar. Pet. Geol.* **2015**, *62*, 1–13. [[CrossRef](#)]
11. Yao, Y.B.; Liu, D.M.; Tang, D.Z.; Tang, S.H.; Huang, W.H.; Liu, Z.H.; Che, Y. Fractal characterization of seepage-pores of coals from China: An investigation on permeability of coals. *Comput. Geosci.* **2009**, *35*, 1159–1166. [[CrossRef](#)]
12. Tian, H.; Pan, L.; Xiao, X.M.; Wilkins, R.W.T.; Meng, Z.P.; Huang, B.J. A preliminary study on the pore characterization of Lower Silurian black shales in the Chuandong Thrust Fold Belt, southwestern China using low pressure N<sub>2</sub> adsorption and FE-SEM methods. *Mar. Pet. Geol.* **2013**, *48*, 8–19. [[CrossRef](#)]
13. Liang, L.X.; Xiong, J.; Liu, X.J. An investigation of the fractal characteristics of the Upper Ordovician Wufeng Formation shale using nitrogen adsorption analysis. *J. Nat. Gas Sci. Eng.* **2015**, *27*, 402–409. [[CrossRef](#)]
14. Yang, C.; Zhang, J.C.; Wang, X.Z.; Tang, X.; Chen, Y.C.; Jiang, L.L.; Gong, X. Nanoscale pore structure and fractal characteristics of a marine-continental transitional shale: A case study from the lower Permian Shanxi Shale in the southeastern Ordos Basin, China. *Mar. Pet. Geol.* **2017**, *88*, 54–68. [[CrossRef](#)]
15. Shao, X.H.; Pang, X.Q.; Li, Q.W.; Wang, P.W.; Chen, D.; Shen, W.B.; Zhao, Z.F. Pore structure and fractal characteristics of organic-rich shales: A case study of the lower Silurian Longmaxi shales in the Sichuan Basin, SW China. *Mar. Pet. Geol.* **2017**, *80*, 192–202. [[CrossRef](#)]
16. Bu, H.L.; Ju, Y.W.; Tan, J.Q.; Wang, G.C.; Li, X.S. Fractal characteristics of pores in non-marine shales from the Huainan coalfield, eastern China. *J. Nat. Gas Sci. Eng.* **2015**, *24*, 166–177. [[CrossRef](#)]
17. Mandelbrot, B.B. Stochastic models for the Earth's relief, the shape and the fractal dimension of the coastlines, and the number-area rule for islands. *Proc. Natl. Acad. Sci. USA* **1975**, *72*, 3825–3828. [[CrossRef](#)]
18. Pfeifer, P. Chemistry in noninteger dimensions between two and three. I. Fractal theory of heterogeneous surfaces. *J. Chem. Phys.* **1984**, *80*, 4573. [[CrossRef](#)]
19. Schluter, E.M.; Zimmerman, R.W. The fractal dimension of pores in sedimentary rocks and its influence on permeability. *Eng. Geol.* **1997**, *48*, 199–215. [[CrossRef](#)]
20. Yao, Y.B.; Liu, D.M.; Tang, D.Z.; Tang, S.H.; Huang, W.H. Fractal characterization of adsorption-pores of coals from North China: An investigation on CH<sub>4</sub> adsorption capacity of coals. *Int. J. Coal Geol.* **2008**, *73*, 27–42. [[CrossRef](#)]
21. Javadpour, F. Nanopores and Apparent Permeability of Gas Flow in Mudrocks (Shales and Siltstone). *J. Can. Pet. Technol.* **2009**, *48*, 16–21. [[CrossRef](#)]
22. Liu, J.Z.; Zhu, J.F.; Cheng, J.; Zhou, J.H.; Cen, K.F. Pore structure and fractal analysis of Ximeng lignite under microwave irradiation. *Fuel* **2015**, *146*, 41–50. [[CrossRef](#)]
23. Ji, W.M.; Song, Y.; Jiang, Z.X.; Meng, M.M.; Liu, Q.X.; Chen, L.; Wang, P.F.; Gao, F.L.; Huang, H.X. Fractal characteristics of nano-pores in the Lower Silurian Longmaxi shales from the Upper Yangtze Platform, south China. *Mar. Pet. Geol.* **2016**, *78*, 88–98. [[CrossRef](#)]
24. Slatt, R.M.; Rodriguez, N.D. Comparative sequence stratigraphy and organic geochemistry of gas shales: Commonality or coincidence? *J. Nat. Gas Sci. Eng.* **2012**, *8*, 68–84. [[CrossRef](#)]
25. Wang, G.C.; Carr, T.R. Methodology of organic-rich shale lithofacies identification and prediction: A case study from Marcellus Shale in the Appalachian basin. *Comput. Geosci.* **2012**, *49*, 151–163. [[CrossRef](#)]
26. Loucks, R.G.; Ruppel, S.C. Mississippian Barnett Shale: Lithofacies and depositional setting of a deep-water shale-gas succession in the Fort Worth Basin, Texas. *AAPG Bull.* **2007**, *91*, 579–601. [[CrossRef](#)]
27. Tan, J.Q.; Weniger, P.; Krooss, B.; Merkel, A.; Horsfield, B.; Zhang, J.C.; Boreham, C.J.; van Graas, G.; Tocher, B.A. Shale gas potential of the major marine shale formations in the Upper Yangtze Platform, South China, Part II: Methane sorption capacity. *Fuel* **2014**, *129*, 204–218. [[CrossRef](#)]

28. Tang, X.L.; Jiang, Z.X.; Huang, H.X.; Jiang, S.; Yang, L.; Xiong, F.Y.; Chen, L.; Feng, J. Lithofacies characteristics and its effect on gas storage of the Silurian Longmaxi marine shale in the southeast Sichuan Basin, China. *J. Nat. Gas Sci. Eng.* **2016**, *28*, 338–346. [[CrossRef](#)]
29. Chen, L.; Lu, Y.C.; Jiang, S.; Li, J.Q.; Guo, T.L.; Luo, C. Heterogeneity of the Lower Silurian Longmaxi marine shale in the southeast Sichuan Basin of China. *Mar. Petrol. Geol.* **2015**, *65*, 232–246. [[CrossRef](#)]
30. Gao, F.L.; Song, Y.; Li, Z.; Xiong, F.Y.; Chen, L.; Zhang, Y.H.; Liang, Z.K.; Zhang, X.X.; Chen, Z.Y.; Joachim, M. Lithofacies and reservoir characteristics of the Lower Cretaceous continental Shahezi Shale in the Changling Fault Depression of Songliao Basin, NE China. *Mar. Petrol. Geol.* **2018**, *98*, 401–421. [[CrossRef](#)]
31. Cai, Q.S.; Hu, M.Y.; Ngia, N.R.; Hu, Z.G. Sequence stratigraphy, sedimentary systems and implications for hydrocarbon exploration in the northern Xujiaweizi Fault Depression, Songliao Basin, NE China. *J. Pet. Sci. Eng.* **2017**, *152*, 471–494. [[CrossRef](#)]
32. Huang, W.B.; Lu, S.F.; Osman, S.H. Quality grading system for tight sandstone reservoirs in the Quantou 4 Member, southern Songliao Basin, Northeast China. *Interpret. J. Sub.* **2017**, *5*, T503–T522. [[CrossRef](#)]
33. Ding, X.Q.; Hersi, O.S.; Hu, X.; Zhu, Y.; Zhang, S.N.; Miao, C.S. Diagenesis of volcanic-rich tight sandstones and conglomerates: A case study from Cretaceous Yingcheng Formation, Changling Sag, Songliao Basin, China. *Arab. J. Geosci.* **2018**, *11*, 287. [[CrossRef](#)]
34. Lin, J.H.; Jiang, T.; Song, L.B.; Cao, Y.; Xia, D.; Wang, Y. The origin and gas vertical distribution of the Harjin mixed-gas reservoir. *Acta Pet. Sin.* **2010**, *34*, 927–932.
35. Jarvie, D.M.; Claxton, B.L.; Henk, F.B.; Breyer, J.T. Oil and Shale Gas from the Barnett Shale, Ft. Worth Basin, Texas, AAPG National Convention, June 3–6, 2001, Denver, CO. *AAPG Bull.* **2001**, *85*, 100.
36. Jarvie, D.M.; Hill, R.J.; Pollastro, R.M. Assessment of the gas potential and yields from shales: The Barnett Shale model. *Oklahoma Geol. Surv. Circ.* **2005**, *110*, 37–50.
37. Ufer, K.; Stanjek, H.; Roth, G.; Dohrmann, R.; Kleeberg, R.; Kaufhold, S. Quantitative phase analysis of bentonites by the Rietveld method. *Clays Clay Miner.* **2008**, *56*, 272–282. [[CrossRef](#)]
38. Curtis, M.E.; Cardott, B.J.; Sondergeld, C.H.; Rai, C.S. Development of organic porosity in the Woodford Shale with increasing thermal maturity. *Int. J. Coal Geol.* **2012**, *103*, 26–31. [[CrossRef](#)]
39. Tang, X.L.; Jiang, Z.X.; Jiang, S.; Li, Z. Heterogeneous nanoporosity of the Silurian Longmaxi Formation shale gas reservoir in the Sichuan Basin using the QEMSCAN, FIB-SEM, and nano-CT methods. *Mar. Petrol. Geol.* **2016**, *78*, 99–109. [[CrossRef](#)]
40. Jiao, K.; Ye, Y.H.; Liu, S.G.; Ran, B.; Deng, B.; Li, Z.W.; Li, J.X.; Yong, Z.Q.; Sun, W. Characterization and Evolution of Nanoporosity in Superdeeply Buried Shales: A Case Study of the Longmaxi and Qiongzhusi Shales from MS Well #1, North Sichuan Basin, China. *Energy Fuels* **2018**, *32*, 191–203.
41. Guo, T.L.; Zhang, H.R. Formation and enrichment mode of Jiaoshiba shale gas field, Sichuan Basin. *Pet. Explor. Dev.* **2014**, *41*, 31–40. [[CrossRef](#)]
42. Sing, K.S. Reporting physisorption data for gas/solid systems with special reference to the determination of surface area and porosity (Recommendations 1984). *Pure Appl. Chem.* **1985**, *57*, 603–619. [[CrossRef](#)]
43. Gao, Z.Y.; Hu, Q.H. Wettability of Mississippian Barnett Shale samples at different depths: Investigations from directional spontaneous imbibition. *AAPG Bull.* **2016**, *100*, 101–114. [[CrossRef](#)]
44. Chen, L.; Jiang, Z.X.; Liu, K.Y.; Tan, J.Q.; Gao, F.L.; Wang, P.F. Pore structure characterization for organic-rich Lower Silurian shale in the Upper Yangtze Platform, South China: A possible mechanism for pore development. *J. Nat. Gas Sci. Eng.* **2017**, *46*, 1–15. [[CrossRef](#)]
45. Wei, Z.F.; Wang, Y.L.; Wang, G.; Sun, Z.P.; Xu, L. Pore characterization of organic-rich Late Permian Da-long Formation shale in the Sichuan Basin, southwestern China. *Fuel* **2018**, *211*, 507–516. [[CrossRef](#)]
46. Wang, Q.T.; Lu, H.; Wang, T.L.; Liu, D.Y.; Peng, P.A.; Zhan, X.; Li, X.Q. Pore characterization of Lower Silurian shale gas reservoirs in the Middle Yangtze region, central China. *Mar. Pet. Geol.* **2018**, *89*, 14–26. [[CrossRef](#)]
47. Fu, H.J.; Wang, X.Z.; Zhang, L.X.; Gao, R.M.; Li, Z.T.; Xu, T.; Zhu, X.L.; Xu, W.; Li, Q. Investigation of the factors that control the development of pore structure in lacustrine shale: A case study of block X in the Ordos Basin, China. *J. Nat. Gas Sci. Eng.* **2015**, *26*, 1422–1432. [[CrossRef](#)]
48. Jiang, F.J.; Chen, D.; Wang, Z.F.; Xu, Z.Y.; Chen, J.; Liu, L.; Huyan, Y.Y.; Liu, Y. Pore characteristic analysis of a lacustrine shale: A case study in the Ordos Basin, NW China. *Mar. Pet. Geol.* **2016**, *73*, 554–571. [[CrossRef](#)]
49. Curtis, M.E.; Sondergeld, C.H.; Ambrose, R.J.; Rai, C.S. Microstructural investigation of gas shales in two and three dimensions using nanometer-scale resolution imaging. *AAPG Bull.* **2012**, *96*, 665–677. [[CrossRef](#)]

50. Milliken, K.L.; Rudnicki, M.; Awwiller, D.N.; Zhang, T. Organic matter-hosted pore system, Marcellus Formation (Devonian), Pennsylvania. *AAPG Bull.* **2013**, *97*, 177–200. [[CrossRef](#)]
51. Yang, R.; He, S.; Yi, J.Z.; Hu, Q.H. Nano-scale pore structure and fractal dimension of organic-rich Wufeng-Longmaxi shale from Jiaoshiha area, Sichuan Basin: Investigations using FE-SEM, gas adsorption and helium pycnometry. *Mar. Pet. Geol.* **2016**, *70*, 27–45. [[CrossRef](#)]
52. Wu, S.T.; Zhu, R.K.; Cui, J.G.; Cui, J.W.; Bai, B.; Zhang, X.X.; Jin, X.; Zhu, D.S.; You, J.C.; Li, X.H. Characteristics of lacustrine shale porosity evolution, Triassic Chang 7 Member, Ordos Basin, NW China. *Pet. Explor. Dev.* **2015**, *42*, 185–195. [[CrossRef](#)]
53. Lu, J.M.; Ruppel, S.C.; Rowe, H.D. Organic matter pores and oil generation in the Tuscaloosa marine shale. *AAPG Bull.* **2015**, *99*, 333–357. [[CrossRef](#)]
54. Jarvie, D.M.; Hill, R.J.; Ruble, T.E.; Pollastro, R.M. Unconventional shale-gas systems: The Mississippian Barnett Shale of north-central Texas as one model for thermogenic shale-gas assessment. *AAPG Bull.* **2007**, *91*, 475–499. [[CrossRef](#)]
55. Li, T.W.; Jiang, Z.X.; Li, Z.; Wang, P.F.; Xu, C.L.; Liu, G.H.; Su, S.Y.; Ning, C.X. Continental shale pore structure characteristics and their controlling factors: A case study from the lower third member of the Shahejie Formation, Zhanhua Sag, Eastern China. *J. Nat. Gas. Sci. Eng.* **2017**, *45*, 670–692. [[CrossRef](#)]



© 2019 by the authors. Licensee MDPI, Basel, Switzerland. This article is an open access article distributed under the terms and conditions of the Creative Commons Attribution (CC BY) license (<http://creativecommons.org/licenses/by/4.0/>).